IJMMM International Journal of Minerals, Metallurgy and Materials 矿物冶金与材料学报（英文版）

NO_2 gas sensor with high selectivity and fast response based on Pt-loaded nanoporous GaN

Dan Han, Xiaoru Liu, Donghui Li, Jiexu Shi, Yu Wang, Yuxuan Wang, Hongtao Wang, and Shengbo Sang

Cite this article as:
Dan Han, Xiaoru Liu, Donghui Li, Jiexu Shi, Yu Wang, Yuxuan Wang, Hongtao Wang, and Shengbo Sang, NO_2 gas sensor with high selectivity and fast response based on Pt-loaded nanoporous GaN, *Int. J. Miner. Metall. Mater.*, 32(2025), No. 4, pp. 964-972. https://doi.org/10.1007/s12613-024-2959-8

View the article online at SpringerLink or IJMMM Webpage.

Articles you may be interested in

Natpichan Pienutsa, Krittamet Yannawibut, Jetthana Phattharaphongmanee, Oukrit Thongananantakul, and Sira Srinives, Titanium dioxide-graphene composite electrochemical sensor for detection of hexavalent chromium, *Int. J. Miner. Metall. Mater.*, 29(2022), No. 3, pp. 529-535. https://doi.org/10.1007/s12613-021-2338-7

Junlian Wang, Lu Liu, Wen Xu, Hui Liu, Guodong Xu, Kun Huang, Fengshan Yu, and Guoyong Huang, Separation of Pd and Pt from highly acidic leach liquor of spent automobile catalysts with monothio-Cyanex 272 and trioctylamine, *Int. J. Miner. Metall. Mater.*, 30(2023), No. 5, pp. 877-885. https://doi.org/10.1007/s12613-022-2492-6

Leyi Zhang, Hongyu Jin, Hanxin Liao, Rao Zhang, Bochong Wang, Jianyong Xiang, Congpu Mu, Kun Zhai, Tianyu Xue, and Fusheng Wen, Ultra-broadband microwave absorber and high-performance pressure sensor based on aramid nanofiber, polypyrrole and nickel porous aerogel, *Int. J. Miner. Metall. Mater.*, 31(2024), No. 8, pp. 1912-1921. https://doi.org/10.1007/s12613-023-2820-5

Shaorou Ke, Yajing Zhao, Xin Min, Yanghong Li, Ruiyu Mi, Yangai Liu, Xiaowen Wu, Minghao Fang, and Zhaohui Huang, Highly mass activity electrocatalysts with ultralow Pt loading on carbon black for hydrogen evolution reaction, *Int. J. Miner. Metall. Mater.*, 32(2025), No. 1, pp. 182-190. https://doi.org/10.1007/s12613-024-2912-x

Shuaishuai Xiao, Jialong Shen, Jianing Zhao, Jie Fang, Caiyu Liang, and Lei Zhou, Electromagnetic responses on microstructures of duplex stainless steels based on 3D cellular and electromagnetic sensor finite element models, *Int. J. Miner. Metall. Mater.*, 31(2024), No. 12, pp. 2681-2691. https://doi.org/10.1007/s12613-024-2894-8

Chao Tan, Junling Lü, Chunchi Zhang, Dong Liang, Lei Yang, and Zegao Wang, Force and impulse multi-sensor based on flexible gate dielectric field effect transistor, *Int. J. Miner. Metall. Mater.*, 32(2025), No. 1, pp. 214-220. https://doi.org/10.1007/s12613-024-2968-7

IJMMM WeChat

QQ author group

INTERNATIONAL JOURNAL OF
Minerals, Metallurgy and Materials

Volume 32, Number 4, April 2025
Page 964

Research Article https://doi.org/10.1007/s12613-024-2959-8

NO_2 gas sensor with high selectivity and fast response based on Pt-loaded nanoporous GaN

Dan Han[1,2),*], *Xiaoru Liu*[1,2),*], *Donghui Li*[1,2,3)], *Jiexu Shi*[1,2)], *Yu Wang*[1,2)], *Yuxuan Wang*[1,2)], *Hongtao Wang*[1,2)], *and Shengbo Sang*[1,2),✉]

1) Shanxi Key Laboratory of Micro/Nano Sensors & Artificial Intelligence Perception, College of Integrated Circuits, Taiyuan University of Technology, Taiyuan 030024, China
2) Key Lab of Advanced Transducers and Intelligent Control System of the Ministry of Education, Taiyuan University of Technology, Taiyuan 030024, China
3) Shanxi Research Institute of 6D Artificial Intelligence Biomedical Science, Taiyuan 030032, China

(Received: 22 February 2024; revised: 19 June 2024; accepted: 24 June 2024)

Abstract: In this work, we realized a room-temperature nitrogen dioxide (NO_2) gas sensor based on a platinum (Pt)-loaded nanoporous gallium nitride (NP-GaN) sensing material using the thermal reduction method and coreduction with the catalysis of polyols. The gas sensor gained excellent sensitivity to NO_2 at a concentration range of 200 ppm to 100 ppb, benefiting from the loading of Pt nanoparticles, and exhibited a short response time (22 s) and recovery time (170 s) to 100 ppm of NO_2 at room temperature with excellent selectivity to NO_2 compared with other gases. This phenomenon was attributed to the spillover effect and the synergic electronic interaction with semiconductor materials of Pt, which not only provided more electrons for the adsorption of NO_2 molecules but also occupied effective sites, causing poor sites for other gases. The low detection limit of Pt/NP-GaN was 100 ppb, and the gas sensor still had a fast response 70 d after fabrication. Besides, the gas-sensing mechanism of the gas sensor was further elaborated to determine the reason leading to its improved properties. The significant spillover impact and oxygen dissociation of Pt provided advantages to its synergic electronic interaction with semiconductor materials, leading to the improvement of the gas properties of gas sensors.

Keywords: nanoporous gallium nitride; platinum; nitrogen dioxide; gas sensor

1. Introduction

Nitrogen dioxide (NO_2) is one of the most critical gaseous pollutants affecting human health, global ecology, and climate change and is a typical atmospheric nitrogen gas marker [1]. Once the oxidation reaction of NO_2 occurs, its reaction products (nitrite and nitrate) pollute the environment, causing a reduction in crop yield and eutrophication [2]. The particulate matter produced by the reaction between NO_2 and volatile organic compounds is a severe pollutant [3]. Moreover, NO_2 commonly induces human respiratory diseases and is one of the marker gases in human disease detection. Studies have shown that long-term exposure to NO_2 can increase the risk of high blood pressure, and prolonged NO_2 irritation can cause olfactory damage [4]. Therefore, the detection of NO_2 in the environment and the human body is of great significance, and the development of a NO_2 gas sensor with high selectivity, wide detection range, and high response is highly anticipated.

In recent years, semiconductor gas sensors have attracted increased attention because of their flexible operating temperature, high sensitivity, rapid response/recovery, and repeatability, such as in atmospheric monitoring [5], wearable devices for gas pollutant monitoring [6], and human disease monitoring [7]. Silicon (Si) field-effect transistors represent conventional gas sensors with their well-established techniques and properties [8]. However, because of the inadequate chemical stability and the narrow band gap (≈1.4 eV) of Si, the potential risk of sensor failure arises. In contrast, wide-band-gap semiconductors (>2 eV) show better chemical properties, such as Si carbide and gallium nitride (GaN). GaN has been widely used in new energy industries because of its wide band gap (0.7–6.1 eV) and excellent temperature stability.

Nowadays, the application of GaN to gas sensing is also anticipated. GaN grown on sapphire and Si through metal–organic chemical vapor deposition not only guarantees excellent gas-sensing characteristics but also demonstrates potential applications for integrated circuits. For example, our group successfully synthesized Au–GaN nanofilms with controllable morphology and gained a low theoretical limit of detection (72 ppb) of ammonia (NH_3). Further, we designed an integration application for gas sensors [9]. Meanwhile, P-type GaN prepared through pulsed-laser abla-

---

* These authors contributed equally to this work.

✉ Corresponding author: Shengbo Sang E-mail: sunboa-sang@tyut.edu.cn

Springer

tion in a liquid was deposited onto a porous Si substrate for a NO_2 gas sensor [10]. It showed a response time of 13.5 s with the limit of detection of 2 ppm at 250°C. Although the sensor exhibited a fast response, the theoretical limit was not enough to satisfy the current requirement. Thus, a NO_2 gas sensor with a lower limit of detection is needed.

As one of the most effective ways to improve the gas-sensing properties of various detectors, precious metal decorations, such as aurum (Au) [11], argentum (Ag) [12], and platinum (Pt), have been widely used in selective detection of gases. Among these materials, Pt has a synergic electronic interaction with semiconductor materials, resulting from its significant spillover impact and oxygen dissociation. Thus, it has been proven to promote the NO_2 gas-sensing performance of composites, even reducing the optimized operating temperature [13–15]. In this regard, Zhao *et al.* [16] fabricated MoS_2 flakes with Pt doping. Their results showed that their gas sensor had a low detection limit of 0.1 ppm and a fast response/recovery time of 35 s/210 s to 32 ppm NO_2 at 157°C. Meanwhile, Shin *et al.* [17] demonstrated a NO_2 gas sensor based on 2D-WS_2 nanofilms with Pt nanoparticles. The gas sensor had a response rate of 47% to 100-ppb NO_2 and showed almost complete recovery (~93.2%) and remarkable repeatability.

In this study, we realized a Pt-loaded nanoporous gallium nitride (Pt/NP-GaN) gas sensor with high selectivity and fast response to NO_2 through the successful doping of Pt nanoparticles [15]. The method included the thermal reduction method to obtain NP-GaN and composite reaction between NP-GaN and Pt with the catalysis of polyols. As anticipated, the limit of detection reached 100 ppb at room temperature (RT) and exhibited a fast response to NO_2 of different concentrations. The morphology, structure, and composition were characterized, and the influence of the loading of Pt on sensing performance was discussed. Moreover, the mechanism of the NO_2 gas sensor was studied on the basis of the potential barrier and electron depletion layer model.

2. Experimental

2.1. Synthesis of NP-GaN and Pt/NP-GaN

Chemicals for the preparation and composite of gas-sensing materials were obtained from Shanghai Macklin Biochemical Technology Co., Ltd: gallium oxide (Ga_2O_3, 99.999%, Shanghai Aladdin Biochemical Technology Co., Ltd), chloroplatinic acid hexahydrate (H_2PtCl_6, 99.9%), polyvinylpyrrolidone (PVP, $(C_6H_9NO)_n$, average molecular weight: 1300000), and triethylene glycol ($C_6H_{14}O_4$). The measurement unit of the gas flow rate was the gas passing volume through the path per minute, simplified as sccm.

The NP-GaN used for the composite was synthesized using the thermal reduction method. The Ga_2O_3 powder was placed into the central temperature zone of a tubular Muffle furnace. The tubular furnace was heated at 10°C/s to 900°C. Then, 40 sccm of N_2 was piped in the zone with the temperature kept at 900°C for 20 min. Thereafter, the furnace was heated at 10°C/s to 1050°C and kept for 120 min. When the temperature reached 1050°C, 150 sccm of NH_3 was piped in. During this process, 40 sccm of N_2 was maintained until the reaction finished. Finally, the furnace was naturally annealed to RT. So far, the NP-GaN has been successfully synthesized.

Pt/NP-GaN microblocks were synthesized using the coreduction method with the catalysis of polyols [18]. Before preparing the composite, we dissolved 50 mg of H_2PtCl_6 in 50 mL of deionized water to obtain 1 mg/mL of a H_2PtCl_6 solution. Then, 50 mg of PVP and 10 mL of $C_6H_{14}O_4$ were mixed in a beaker as a reaction environment. After being stirred evenly, the mixture was heated to 200°C in an oil bath. Then, 2 ml of the H_2PtCl_6 solution and 50 mg of NP-GaN were mixed and poured into the reaction solution when the temperature of the reaction solution reached 200°C. The solution was stirred and kept at 200°C for 1 h. After cooling to RT, acetone was added to the mixture, which was then centrifuged to remove the chemical residue. This step was repeated after replacing acetone with ethanol and deionized water separately. Finally, the sediment was dried to obtain the target material. The amounts of the H_2PtCl_6 solution were varied (5 and 10 mL) to synthesize Pt/NP-GaN with different Pt loads. The Pt/NP-GaN composites with 2, 5 and 10 mL of the H_2PtCl_6 solution were labeled as Pt/NP-GaN-1, Pt/NP-GaN-2, and Pt/NP-GaN-3, respectively.

The Pt/NP-GaN synthesized through these steps was powdery, and the material was dispersed in deionized water through ultrasonication for 20 min. Then, the mixture was dropped onto a silver electrode and dried at 60°C. Thus, a simple gas sensor was fabricated.

2.2. Measurement of gas sensing

In this test, the CGS-MT probe station combined with the SA3102 source and measurement unit was used for gas detection, and the applied voltage of the tests was 1000 mV. All measurements were taken at 101 kPa. The standard NO_2 gas (≥99.99%) was the target gas made through the vaporization of liquid NO_2. The concentration of the target gas (C) was calculated using the following formula:

$$V_x = \frac{V \times C \times M}{22.4 \times d \times p} \times 10^{-9},$$

where V_x is the solution volume of the target gas, V is the volume of the chamber, M is the molecular weight of the target gas, d is the density of the solution, and p is the concentration of the solution. A certain amount of NO_2 mixed with pure air was injected into the gas chamber; therefore, the gas-sensing properties could be detected. In the test of selectivity, ethanol, *n*-butanol, NH_3, and acetone were injected into the microheater using Microliter Syringes and evaporated into gas.

The response of the gas-sensing material was defined as the ratio of the resistance change after the target gas was injected to the original resistance, expressed by the following formula:

$$S\,(\%) = \frac{|\Delta R|}{R_a} \times 100\%,$$

where ΔR is the change in resistance after the gas sensor is exposed to the target gas, and R_a is the resistance of the sensor in clean air. The response time is defined as the time required to reach 90% of the stable value after the response, whereas the recovery time is defined as the time to reach 10% of the stable baseline response value during desorption.

2.3. Characterizations

X-ray diffraction (XRD) was used to determine the crystal composition of pure GaN and Pt/GaN (Aeris, $\lambda = 1.5418$ Å and 2θ = 20°–80°). Scanning electron microscopy (SEM) equipped with an energy-dispersive spectrometer (EDS) was performed using a JSM-IT500 instrument at an accelerating voltage of 15 kV. Transmission electron microscopy (TEM, JEOL JEM-F200) with an acceleration voltage of 200 kV was also used for further morphological studies. X-ray photoelectron spectroscopy (XPS, Thermo Scientific ESCALAB Xi+) was conducted to analyze the valence state, element composition, and content on the material surface. The test results of the binding energy were corrected and analyzed with carbon at 284.8 eV as the standard.

3. Results and discussion

3.1. Structure, morphology, and composition of Pt/NP-GaN

The phase identification of the samples was determined using XRD, and the results are shown in Fig. 1. Curve a is the XRD pattern of the NP-GaN microblock, whereas curves *b*, *c*, and *d* represent the XRD patterns of Pt/NP-GaN containing different loading amounts of Pt. Apparently, the reflections of all patterns were identified as the reflections of GaN (JCPDS No. 50-0792). Comparing with the others, a new peak centered at 40.04° appeared because of the addition of H_2PtCl_6. It could be assigned to the (111) reflection of Pt (JCPDS No. 01-1194), as shown in Fig. S1 (see the Supplementary Information). The intensity of this peak increased with the increase in loading amount, indicating the effective loading of Pt. Meanwhile, there were no other diffraction peaks in the XRD spectrum, indicating the high purity of the samples.

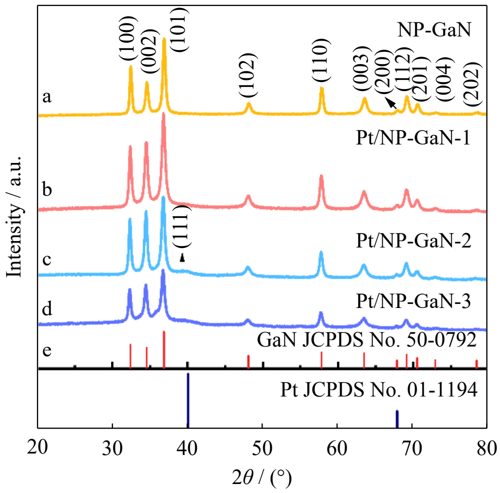

Fig. 1. XRD patterns of NP-GaN and Pt/NP-GaN.

Fig. 2(a) and (b) shows SEM images of Ga_2O_3 and pure NP-GaN, respectively. In contrast to Ga_2O_3, more nanopores can provide sites for adsorption and desorption of gas sensing. The morphology of Pt/NP-GaN-1 and Pt/NP-GaN-2 are shown in Fig. 2(c) and (d), and many nanoparticles are attached to the surface of NP-GaN after catalysis, indicating the successful loading of Pt. Fig. 2(e) depicts the partially enlarged morphology of Pt/NP-GaN-2.

EDS was used to analyze the elements of materials in Fig. 2(f)–(h). As shown in Fig. 2(i) and Fig. S2, the atomic ratios of Pt loaded GaN were 0.585%, 0.434%, and 1.46%, corresponding to Pt/NP-GaN-2, Pt/NP-GaN-1, and Pt/NP-GaN-3, respectively, which satisfied the increase in load capacity. Above all, Pt was successfully loaded on NP-GaN, and we can infer that the nanoporous structure of NP-GaN contributed to the improvement of its gas-sensing properties.

The morphology of the Pt/NP-GaN-2 microblock was examined using TEM, as shown in Fig. 3(a). The microparticle of NP-GaN showed heterogeneous transparency resulting from the nanopores on the surface, which contributed to the increase in the specific surface area in contact with the gas. In Fig. 3(b), the interplanar spacing distance (*d*) of 2.275 Å corresponded to the (111) plane of cubic-phase Pt, whereas the *d* of 2.769 Å fits well with the $(10\bar{1}0)$ planes of the hexagonal GaN [19]. As demonstrated in Fig. 3(c) and (d), the corresponding fast Fourier transform (FFT) pattern verified the high consistency of the NP-GaN and Pt lattice fringes.

The results of the Brunauer–Emmett–Teller (BET) analysis are shown in Table 1 and Fig. S3. The specific surface area of pure NP-GaN and Pt/NP-GaN-2 were 9.672 and 27.539 m^2/g, respectively. Apparently, the specific surface area increased after the loading of Pt nanoparticles, and pores in these two materials existed in the form of mesoporous pores (pore size range from 2 to 50 nm). In this case, the dispersion of Pt on the surface of NP-GaN micro-particles and the increase in specific surface area accelerated the adsorption and desorption processes, thus improve the gas-sensing properties of the tested materials.

The elemental composition and chemical states of the samples were confirmed by XPS spectra. Obviously, Ga, N, C, O, and Pt were clearly analyzed, as shown in Fig. 4(a). Because of the small amount of Pt loading, the characteristic peaks of Pt 4f in the Pt/NP-GaN microblocks were not especially high, whereas the other main peaks of Pt/NP-GaN corresponded to NP-GaN. As shown in Fig. 4(b)–(d), there were no significant deviations between the main peaks of the samples with Pt at different loading concentrations. The Ga 3d peaks of Pt/NP-GaN-1 could be convoluted into three binding energy peak positions of 18.99, 19.99, and 20.99 eV in Fig. 4(b), corresponding to Ga–Ga, Ga–N, and Ga–O, respectively. The N 1s spectrum could be fitted to Ga–LMM and N–Ga at around 396.64 and 397.67 eV in Fig. 4(c) [20]. The XPS spectrum of Pt 4f is shown in Fig. 4(d). The binding energy of Pt $4f_{7/2}$ in the XPS spectra of Pt/GaN-1, Pt/GaN-2, and Pt/GaN-3 were 70.73, 70.69, and 70.80 eV, respectively [21]. Meanwhile, the Pt $4f_{5/2}$ peak at around

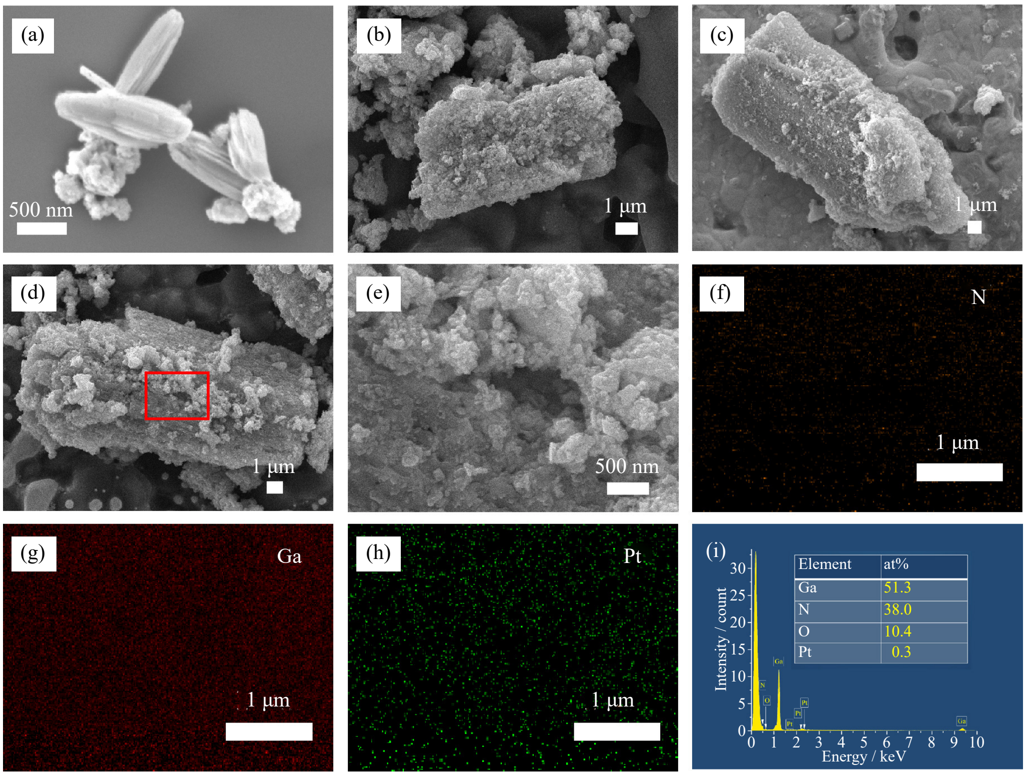

Fig. 2. SEM images of (a) Ga$_2$O$_3$, (b) pure NP-GaN, (c) Pt/NP-GaN-1, and (d) Pt/NP-GaN-2. (e) Partially enlarged image and (f–i) the corresponding EDS energy spectrum of Pt/NP-GaN-2.

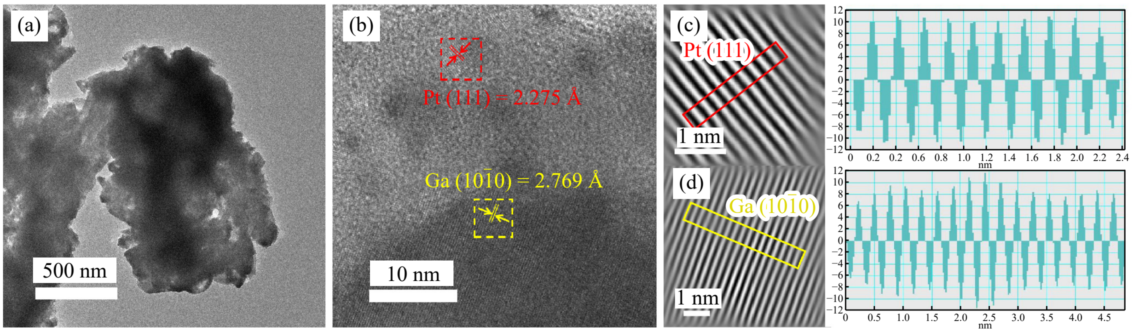

Fig. 3. (a) TEM and (b) high-resolution TEM images of Pt/NP-GaN-2. (c) FFT images and (d) corresponding profiles of FFT to different regions of Pt/NP-GaN-2.

Table 1. BET results of pure NP-GaN and Pt/NP-GaN-2

Materials	Surface area / (m^2·g^{-1})	Pore volume / (cm^3·g^{-1})	Pore size / nm
NP-GaN	9.672	0.0227	9.382
Pt/NP-GaN-2	27.539	0.0551	8.004

73.99 eV contributed to the experimental Pt 4f, thus making the fitted curve conform to the spectra. The binding energy of XPS spectra had varying degrees of shifts because of the transfer of electrons from GaN to Pt through the heterojunction between them. These results conform to previous reports about Pt and confirm the successful loading of Pt in Pt/NP-GaN microblocks.

3.2. Gas-sensing performance

The gas-sensing performances of all samples were tested in our experiments. Because of the insignificant response and unsteadiness of Pt/NP-GaN-1 and Pt/NP-GaN-3, our following research was focused on Pt/NP-GaN-2, and the gas-sensing properties of pure NP-GaN were shown for comparison.

The operating temperature plays an important role in semiconductor gas sensors. At appropriate operating temperatures, the capacity of oxygen absorbed on the surface and the carrier concentration are increased, and the sensing membrane is activated because of the lower activation energy. Therefore, it is crucial to find the optimum operating temperature of gas sensors [22–23]. As depicted in Fig. 5(a), the resistance of Pt/NP-GaN-1 is higher than that of NP-GaN, whereas the resistance of Pt/NP-GaN-2 and Pt/NP-GaN-3 decreased after the loading of Pt nanoparticles. While the loading amount of Pt was in excess, the Pt nanoparticle agglomerated on the surface and formed an independent electron transmission, which caused an intuitionistic decrease in the resistance of Pt/NP-GaN-3 compared with Pt/NP-GaN-2. Moreover, the resistance of Pt/NP-GAN-2 decreased with an increase in operating temperature. This might be attributed to

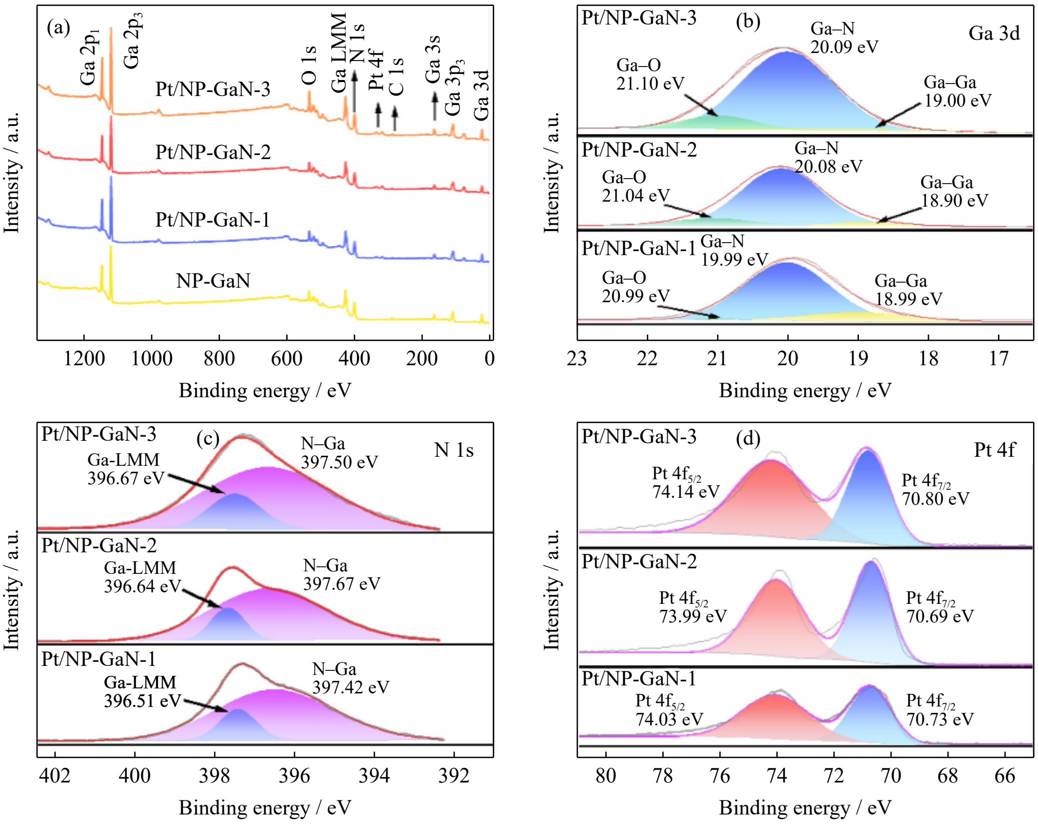

Fig. 4. XPS spectra of Pt/NP-GaN microblocks: (a) full spectrum; (b) Ga 3d; (c) N 1s; (d) Pt 4f.

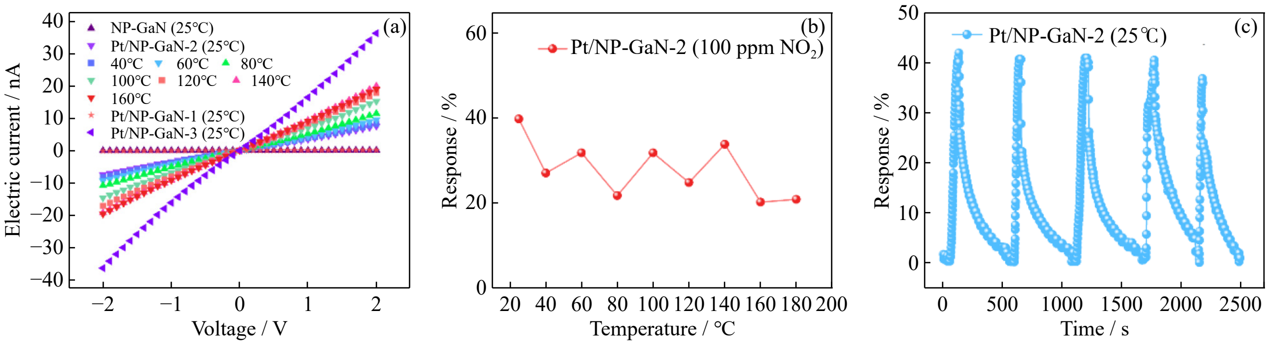

Fig. 5. Dynamic curves: (a) *I–V* characteristic of the four samples; (b) temperature-dependent response to 100 ppm of NO_2 of Pt/NP-GaN-2; (c) repeatability curve of Pt/NP-GaN-2 at RT.

an increased number of electrons excited from the valence band to the conduction band of NP-GaN microblocks as the temperature increased. Thus, the resistance of the gas sensors decreased.

To investigate the influence of the operating temperature on the gas sensors, the response curves of Pt/NP-GaN-2 to 100 ppm of NO_2 at different temperatures are demonstrated in Fig. 5(b). The gas sensor was stable at low temperatures, but its response began to decrease when the temperature reached 160°C. To find the optimum operating temperature of the gas sensor, the repeatability curves to 100 ppm of NO_2 at 25, 80, and 120°C are shown in Fig. 5(c) and Fig. S4. Although the response to 100 ppm of NO_2 at 80°C was initially higher than the others, the response decreased with the increase in the number of tests, which was also at 120°C. The sensor to 100 ppm of NO_2 at 25°C was tested for five cycles, and the change in response between each cycle was negligible with a stable baseline, as shown in Fig. 5(c). As mentioned above, the number of active electrons increased with the increasing temperature. This led to the unstable state of electrons, which meant that the effects of the testing environment, such as the intensity of pressure and vibration, were increased at higher temperatures. Above all, the gas sensor presented the most excellent performance at RT (25°C).

Fig. 6(a) shows the dynamic response of Pt/NP-GaN-2 under NO_2 at various concentrations at RT, and the corresponding curve of resistance change is depicted in Fig. S5. It was found that the response decreased with lower concentrations and fitted the Langmuir fitting curve shown in Fig. 6(b). Notably, the gas sensor had 100 ppb of NO_2 as the lowest detected concentration, with a response of 2.37%.

As important parameters of the performance evaluation, the response time and recovery time were also studied. Fig. 6(c) and (d) depicts the response and recovery curves of

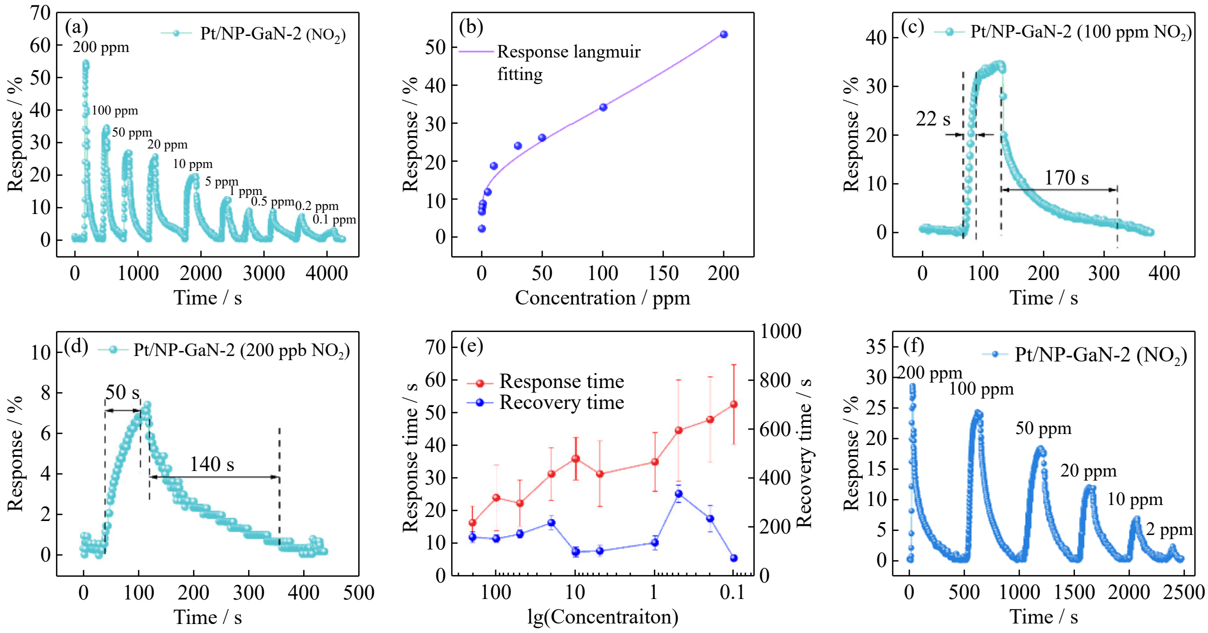

Fig. 6. (a) Dynamic response curve of Pt/NP-GaN-2 to various NO_2 concentrations at 25°C and (b) corresponding Langmuir fitting curve; response curve of the Pt/NP-GaN-2 gas sensor to (c) 100 ppm of NO_2 and (d) 200 ppb of NO_2; (e) curves of the response time and recovery time of Pt/NP-GaN-2 gas sensor for different concentrations of NO_2; (f) response curve of Pt/NP-GaN-2 after 70 d.

Pt/NP-GaN-2 exposed to 100 ppm and 200 ppb of NO_2 at RT, respectively. The Pt/NP-GaN-2 sensor displayed a quick response to NO_2 of different concentrations.

Fig. 6(e) shows the response and recovery trends with the decreasing concentrations of NO_2. Apparently, the response decelerated with the lower concentrations of the gas, whereas the recovery had no significant trend.

To measure the stability of the sensor, the response of Pt/NP-GaN-2 to NO_2 at different concentrations was tested 70 d after synthesis [24]. In Fig. 6(f), the response to 100, 50, 20, 10, and 2 ppm of NO_2 still demonstrated linear change, but the low limit of detection was 5 ppm, which resulted from the long-term adsorption of gas molecules in environments on the surface of the materials, causing less adsorbed sites. As shown in Fig. S6, we tested the repeatability of Pt/NP-GaN-2 for another two samples. Each sample showed great repeatability, which also proved the stability of Pt/NP-GaN to NO_2.

Acetone, alcohol (C_2H_5OH), NH_3, trimethylamine (TMA), and NO_2 were detected to investigate the selectivity of NP-GaN and Pt/NP-GaN-2 at RT. Fig. 7(a) shows their response under acetone, C_2H_5OH, NH_3, TMA, and NO_2 at a concentration of 200 ppm, respectively. Obviously, NP-GaN had a high response to both NH_3 and TMA. Pt/NP-GaN-2 had a higher response to NO_2 compared with the other gases. In Fig. S7(a), Pt/NP-GaN-2 had a faster response and recovery to NO_2 compared with the others. This could be attributed to the existence of Pt nanoparticles in the pores of NP-GaN, which provided sites for adsorbed oxygen molecules but prevented the adsorption of other molecules at the same time, thus improving the selectivity of the gas sensors. Besides, the oxygen molecules adsorbed on the Pt nanoparticles were decomposed to ionized oxygen and diffused to the surface of NP-GaN on account of the spillover effect. In this case, the gas-sensing performance was optimized after the loading of Pt nanoparticles.

Environmental relative humidity (RH), another critical factor that influences the response of gas sensors, was further

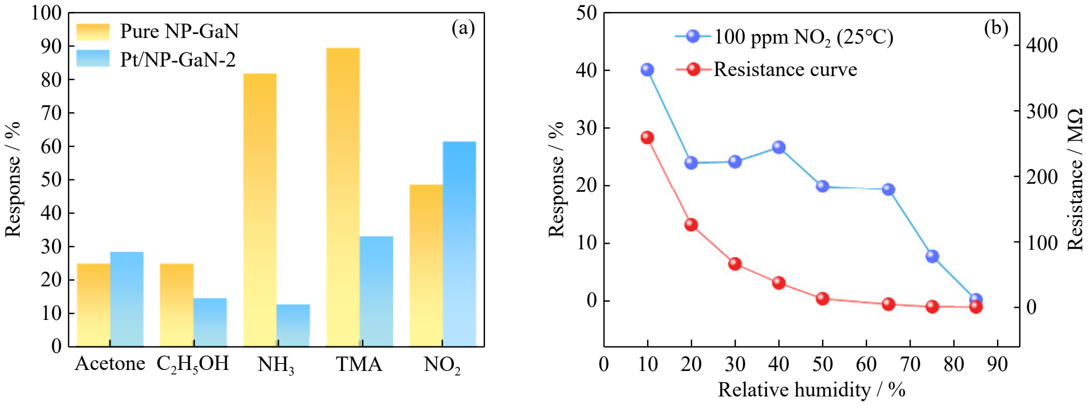

Fig. 7. (a) Response of samples to various gases at 200 ppm and (b) effect of relative humidity on the resistance and response of the gas sensor to 100 ppm of NO_2 at RT.

studied. Fig. 7(b) shows the dynamic resistance and response curve of Pt/NP-GaN-2 at 10%, 20%, 30%, 40%, 50%, 65%, 75%, and 85% RH, and the corresponding resistance curve is displayed in Fig. S7(b). We also repeated the test, and the results are shown in Fig. S7(c). The responses to 100 ppm of NO_2 were 40.11%, 24.04%, 24.24%, 26.71%, 19.9%, 19.33%, 7.71%, and 0.2% as the RH increased. The decreased resistance with the increase in RH slowed down above 70% RH, resulting from the saturation adsorption of water molecules on the surface. Meanwhile, the adsorption of NO_2 molecules was difficult because the more water molecules were absorbed, the less adsorbed sites could be provided for the reaction between chemisorbed oxygen and NO_2 molecules. Thus, the performance of the gas sensor deteriorated [25–26].

Table 2 compares various NO_2 gas sensors. T_{res} and T_{rec} are the response time and recovery time to NO_2 of the concentrations listed in the table, respectively. It can be seen that Pt/NP-GaN-2 exhibited a fast response and recovery compared with the others, indicating the effective loading of Pt nanoparticles.

3.3. Gas-sensing mechanism

The gas-sensing properties of the sensors were analyzed in the section above. The gas reaction mechanism of Pt/NP-GaN to NO_2 is elaborated below.

Because of the higher work function of Pt (4.90 eV) compared with that of GaN (4.2 eV), partial free electrons would transfer from GaN to Pt upon contact between them, forming a new equilibrium of the Fermi energy level and a Schottky junction, as shown in Fig. 8(a) and (b) [23].

Because of the unpaired electrons of the nitrogen atom, NO_2 manifested an electron receptor nature as a strong oxidizing agent [32]. The chemoresistance gas sensor detected the target gas molecules using its sensing layer. Fig. 8(c) and (d) shows the depletion region change of the NP-GaN microblock with and without Pt nanoparticles under different atmospheres. Generally, the adsorption of oxygen molecules (O_2(gas)) happens on the surface of gas-sensing materials. Then, there is a reaction between the adsorbed oxygen molecules (O_2(ads)) and the electron (e^-) attached to the surface, which produces the adsorbed oxygen ions (O_2^-(ads)) on the surface of the gas-sensing materials [33–34]. These steps above are indicated by Eqs. (1) and (2):

$$O_2\,(\text{gas}) \rightarrow O_2\,(\text{ads}) \tag{1}$$

$$O_2\,(\text{ads}) + e^- \rightarrow O_2^-\,(\text{ads}) \tag{2}$$

On this basis, the NO_2 molecules were absorbed on the surface of the gas-sensing materials after they were injected into the air chamber. Because of the existence of O_2^-(ads) and

Table 2. Comparison of reported NO_2 gas sensors

Materials	Work temperature / °C	Concentration / ppm	Response / %	(T_{res}/T_{rec}) / s	Limit of detection	Ref.
SnO_2/graphene	RT	5	8	180/1800	3 ppm	[27]
MoS_2	150	100	40.3	79/225	500 ppb	[28]
GaN/WO_3	300	5	1.8	132/113	1 ppm	[29]
$Ti_3C_2T_x$–ZnO	RT	100	41.93	54/103	5 ppm	[30]
MoS_2/$Ti_3C_2T_x$	RT	20	40	525/155	1 ppm	[31]
Pt/NP-GaN	RT	100	32.6	22/170	100 ppb	This work

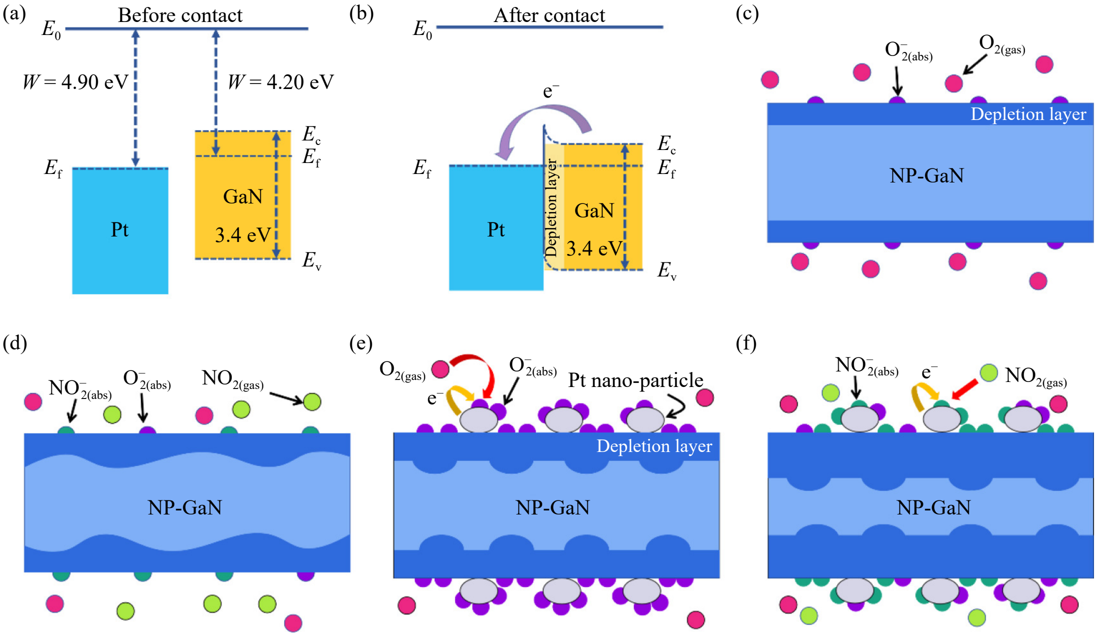

Fig. 8. Energy band diagram of (a) NP-GaN and (b) Pt/NP-GaN; depletion layers of (c) NP-GaN in air and (d) NO_2; Pt/NP-GaN in (e) air and (f) NO_2.

e^- on the surface, the NO_2 molecules reacted with them, as respectively shown in Eqs. (3) and (4) [35–36]:

$$NO_2\,(gas) + e^- \rightarrow NO_2^-\,(ads) \tag{3}$$

$$NO_2\,(gas) + O_2^-\,(ads) + 2e^- \rightarrow NO_2^-\,(ads) + 2O^-\,(ads) \tag{4}$$

The reaction accelerated the extraction of electrons on the surface, leading to a thicker depletion region in the NP-GaN microblock. As shown in Fig. 8(e), more electrons were produced on the surface because of the metal spillover effect after the loading of Pt nanoparticles. Then, the surface potential and barrier height were changed [37]. In that case, more electrons reacted with the O_2^-(ads) on the surface, as shown in Fig. 8(f). Therefore, Pt/NP-GaN had a thicker depletion region than that of pure NP-GaN [38–39]. However, the excessive Pt nanoparticles dominated the resistance of the composites; thus, the resistance of the composites was lower than that of pure NP-GaN. Furthermore, the reactions stated in Eqs. (3) and (4) were intensified after the injection of NO_2, and it caused electrons to be extracted from the surface, which thickened the depletion region. The resistance change of the gas sensors increased, resulting from the thicker depletion layer. In other words, the responses of the gas sensors were increased.

Moreover, the nanoporous structures devoted advantages to the gas-sensing performance by increasing the specific surface area. The nanoporous surfaces provided more sites for the loading of Pt nanoparticles and the contact with NO_2 molecules. In other words, it encouraged the loading of Pt nanoparticles and resulted in better gas-sensing performance.

4. Conclusion

In this paper, Pt-loaded NP-GaN microblocks were successfully synthesized using the thermal reduction method and coreduction method with the catalysis of polyols. Compared with pure NP-GaN, excellent selectivity to NO_2 was realized through the loading of Pt nanoparticles. The Pt/NP-GaN gas sensor demonstrated a stable response (40%) to 100 ppm of NO_2 with a fast response time (≤22 s) at RT. The low limit ofdetection was 100 ppb. Combined with the elaboration of the gas-sensing mechanism, the successful loading of Pt not only provided more electrons for materials to react with NO_2 but also occupied effective sites for adsorption, leading to a special selectivity to NO_2. Meanwhile, the operating temperature ranged from 25 to 140°C with an optimum operating temperature of 25°C, which is of great significance in the further exploration of gas sensors. Above all, this study provides a practicable method for RT and fast response NO_2 gas sensors.

Acknowledgements

This work was supported by the National Natural Science Foundation of China (Nos. 62031022 and 52375572), the Key R&D Program of Shanxi Province, China (No. 202102030201003), Shanxi-Zheda Institute of Advanced Materials and Chemical Engineering, China (No. 2022SX-AT001), and Key Core Technological Breakthrough Program of Taiyuan City, China (No. 2024TYJB0126).

Conflict of Interest

The authors declare that they have no known competing financial interests or personal relationships that could have appeared to influence the work reported in this paper.

Supplementary Information

The online version contains supplementary material available at https://doi.org/10.1007/s12613-024-2959-8.

References

[1] C.X. Zhang, C. Liu, B. Li, F. Zhao, and C.H. Zhao, Spatiotemporal neural network for estimating surface NO_2 concentrations over North China and their human health impact, *Environ. Pollut.*, 307(2022), art. No. 119510.

[2] D.H. Li, D. Han, Y. Chen, *et al.*, Hollow porous GaN nanofibers gas sensor for superior stability and sub-ppb-level NO_2 gas detection, *Sens. Actuat. B: Chem.*, 371(2022), art. No. 132583.

[3] N.A. Amoah, G. Xu, Y. Wang, J.Y. Li, Y.M. Zou, and B.S. Nie, Application of low-cost particulate matter sensors for air quality monitoring and exposure assessment in underground mines: A review, *Int. J. Miner. Metall. Mater.*, 29(2022), No. 8, p. 1475.

[4] M.M.M.F. Jion, J.N. Jannat, M.Y. Mia, *et al.*, A critical review and prospect of NO_2 and SO_2 pollution over Asia: Hotspots, trends, and sources, *Sci. Total Environ.*, 876(2023), art. No. 162851.

[5] O.G. Agbonlahor, M. Muruganathan, S.G. Ramaraj, *et al.*, Interfacial ammonia selectivity, atmospheric passivation, and molecular identification in graphene-nanopored activated carbon molecular-sieve gas sensors, *ACS Appl. Mater. Interfaces*, 13(2021), No. 51, p. 61770.

[6] H. Wan, H.Y. Yin, L. Lin, X.Q. Zeng, and A.J. Mason, Miniaturized planar room temperature ionic liquid electrochemical gas sensor for rapid multiple gas pollutants monitoring, *Sens. Actuat. B: Chem.*, 255(2018), p. 638.

[7] J.L. Zhao, W.F. Shen, D.W. Lv, *et al.*, Gas-sensing technology for human breath detection, *Prog. Chem.*, 35(2023), No. 2, p. 302.

[8] S. Hong, M.L. Wu, Y. Hong, *et al.*, FET-type gas sensors: A review, *Sens. Actuat. B: Chem.*, 330(2021), art. No. 129240.

[9] D. Han, Y. Chen, D.H. Li, *et al.*, Au nanoparticles decorated GaN nanoflowers with enhanced NH_3 sensing performance at room temperature, *Sens. Actuat. B: Chem.*, 394(2023), art. No. 134320.

[10] H.A.A. Abdul Amir, M.A. Fakhri, A.A. Alwahib, E.T. Salim, F.H. Alsultany, and U. Hashim, An investigation on GaN/porous-Si NO_2 gas sensor fabricated by pulsed laser ablation in liquid, *Sens. Actuat. B: Chem.*, 367(2022), art. No. 132163.

[11] J.Y. Hu, J.W. Zhang, X. Liu, H.Y. Zhang, X.X. Xue, and Y. Zhang, Highly selective NO_2 sensor based on Au/SnS_2 nanoheterostructures via visible-light modulation, *Appl. Surf. Sci.*, 623(2023), art. No. 157093.

[12] M.Y. Kim, S.Y. Lee, A. Mirzaei, *et al.*, NO_2 gas sensing properties of Ag-functionalized porous ZnO sheets, *Adsorpt. Sci. Technol.*, 2023(2023), . art. No. 9021169.

[13] S. Kumar, S.D. Lawaniya, S. Agarwal, *et al.*, Optimization of Pt

nanoparticles loading in ZnO for highly selective and stable hydrogen gas sensor at reduced working temperature, *Sens. Actuat. B: Chem.*, 375(2023), art. No. 132943.

[14] M. Wusiman and F. Taghipour, Methods and mechanisms of gas sensor selectivity, *Crit. Rev. Solid State Mater. Sci.*, 47(2022), No. 3, p. 416.

[15] M. Shafa, D. Priante, R.T. ElAfandy, *et al.*, Twofold porosity and surface functionalization effect on Pt-porous GaN for high-performance H_2-gas sensors at room temperature, *ACS Omega*, 4(2019), No. 1, p. 1678.

[16] W.J. Zhao, R.T. Yan, H. Li, K.L. Ding, Y.S. Chen, and D. Xu, Highly sensitive NO_2 gas sensor with a low detection limit based on Pt-modified MoS_2 flakes, *Mater. Lett.*, 330(2023), art. No. 133386.

[17] D. Shin, I. Sohn, J. Kim, *et al.*, Defect-selective functionalization of 2D-WS_2 nanofilms with Pt nanoparticles for enhanced room-temperature NO_2 gas sensing, *ACS Appl. Nano Mater.*, 6(2023), No. 20, p. 19327.

[18] Y.L. Wang, Z.Q. Liu, L. Yang, *et al.*, Highly selective gas sensor for rapid detection of triethylamine using PdRu alloy nanoparticles functionalized SnO_2, *Sens. Actuat. B: Chem.*, 379(2023), art. No. 133205.

[19] J.J. Liu, L.Y. Zhang, J.J. Fan, B.C. Zhu, and J.G. Yu, Triethylamine gas sensor based on Pt-functionalized hierarchical ZnO microspheres, *Sens. Actuat. B: Chem.*, 331(2021), art. No. 129425.

[20] I. Susanto, C.Y. Tsai, Fachruddin, *et al.*, The influence of 2D MoS_2 layers on the growth of GaN films by plasma-assisted molecular beam epitaxy, *Appl. Surf. Sci.*, 496(2019), art. No. 143616.

[21] M. Sarno and E. Ponticorvo, Much enhanced electrocatalysis of Pt/PtO_2 and low platinum loading Pt/PtO_2–Fe_3O_4 dumbbell nanoparticles, *Int. J. Hydrogen Energy*, 42(2017), No. 37, p. 23631.

[22] K. Shingange, H.C. Swart, and G.H. Mhlongo, Design of porous p-type $LaCoO_3$ nanofibers with remarkable response and selectivity to ethanol at low operating temperature, *Sens. Actuat. B: Chem.*, 308(2020), art. No. 127670.

[23] H.T. Wang, Y.Y. Li, C.C. Wang, *et al.*, N-pentanol sensor based on ZnO nanorods functionalized with Au catalysts, *Sens. Actuat. B: Chem.*, 339(2021), art. No. 129888.

[24] Y.H. Gui, Y.S. Tu, H.S. Guo, *et al.*, Microwave-assisted efficient synthesis of ZnO nanospheres for low temperature NO_2 gas sensor, *Mater. Sci. Eng. B*, 299(2024), art. No. 117031.

[25] H.N. Bai, H. Guo, J. Wang, *et al.*, A room-temperature NO_2 gas sensor based on CuO nanoflakes modified with rGO nanosheets, *Sens. Actuat. B: Chem.*, 337(2021), art. No. 129783.

[26] H.N. Bai, H. Guo, J. Wang, *et al.*, Hydrogen gas sensor based on SnO_2 nanospheres modified with Sb_2O_3 prepared by one-step solvothermal route, *Sens. Actuat. B: Chem.*, 331(2021), art. No. 129441.

[27] L.Z. Zhang, J.N. Shi, Y.H. Huang, *et al.*, Octahedral SnO_2/graphene composites with enhanced gas-sensing performance at room temperature, *ACS Appl. Mater. Interfaces*, 11(2019), No. 13, p. 12958.

[28] Y.X. Li, Z.X. Song, Y.N. Li, *et al.*, Hierarchical hollow MoS_2 microspheres as materials for conductometric NO_2 gas sensors, *Sens. Actuat. B: Chem.*, 282(2019), p. 259.

[29] S. Park, H. Ko, S. Kim, and C.M. Lee, Gas sensing properties of multiple networked GaN/WO_3 core–shell nanowire sensors, *Ceram. Int.*, 40(2014), No. 6, p. 8305.

[30] Z.J. Yang, L. Jiang, J. Wang, *et al.*, Flexible resistive NO_2 gas sensor of three-dimensional crumpled MXene $Ti_3C_2T_x$/ZnO spheres for room temperature application, *Sens. Actuat. B: Chem.*, 326(2021), art. No. 128828.

[31] Q. Thanh Hoai Ta, N. Ngoc Tri, and J.S. Noh, Improved NO_2 gas sensing performance of 2D MoS_2/$Ti_3C_2T_x$ MXene nanocomposite, *Appl. Surf. Sci.*, 604(2022), art. No. 154624.

[32] A.V. Agrawal, N. Kumar, and M. Kumar, Strategy and future prospects to develop room-temperature-recoverable NO_2 gas sensor based on two-dimensional molybdenum disulfide, *Nano Micro Lett.*, 13(2021), art. No. 38.

[33] S.Y. Chu, M.J. Wu, T.H. Yeh, C.T. Lee, and H. Lee, Sensing mechanism and characterization of NO_2 gas sensors using gold-black NP-decorated Ga_2O_3 nanorod sensing membranes, *ACS Sens.*, 9(2023), No. 1, p. 118.

[34] Y. Yin, Y. Shen, S. Zhao, *et al.*, Enhanced detection of ppb-level NO_2 by uniform Pt-doped $ZnSnO_3$ nanocubes, *Int. J. Miner. Metall. Mater.*, 29(2022), No. 6, p. 1295.

[35] P.J. Cao, Y.Z. Cai, D. Pawar, *et al.*, Down to ppb level NO_2 detection by ZnO/rGO heterojunction based chemiresistive sensors, *Chem. Eng. J.*, 401(2020), art. No. 125491.

[36] Y.S. Xu, J.Y. Xie, Y.F. Zhang, *et al.*, Edge-enriched WS_2 nanosheets on carbon nanofibers boosts NO_2 detection at room temperature, *J. Hazard. Mater.*, 411(2021), art. No. 125120.

[37] N. Sharma, S. Kumar, A. Gupta, *et al.*, MoS_2 functionalized AlGaN/GaN transistor based room temperature NO_2 gas sensor, *Sens. Actuat. A: Phys.*, 342(2022), art. No. 113647.

[38] G. Mathankumar, P. Bharathi, M.K. Mohan, J. Archana, S. Harish, and M. Navaneethan, Defect manipulation of WO_3 nanostructures by yttrium for ultra-sensitive and highly selective NO_2 detection, *Sens. Actuat. B: Chem.*, 353(2022), art. No. 131057.

[39] W.W. Wang, D.Y. Wang, X.X. Zhang, C.Q. Yang, and D.Z. Zhang, Self-powered nitrogen dioxide sensor based on Pd-decorated ZnO/$MoSe_2$ nanocomposite driven by triboelectric nanogenerator, *Nanomaterials*, 12(2022), No. 23, art. No. 4274.